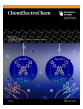

In Situ Electrochemical Investigations of Inherently Chiral 2,2′-Biindole Architectures with Oligothiophene Terminals

Claudia Malacrida[+],[a] Luca Scapinello[+],[a, b] Roberto Cirilli,[c] Sara Grecchi,[d] Andrea Penoni,[b] Tiziana Benincori,*[b] and Sabine Ludwigs*[a]

The synthesis and characterization of three new inherently chiral *N*,*N*′-dipropyl-3,3′-diheteroaryl-2,2′-biindole monomers, nicknamed Ind_2T_4, Ind_2T_6 and $Ind_2Ph_2T_4$, which differ in the number of thiophenes as terminals, are reported. In addition to a full monomer characterization, stable electroactive oligomeric films were obtained by electro-oxidation upon cycling to potentials which activate the thiophene terminals. Cyclic voltammetry, UV-Vis-NIR spectroelectrochemistry and *in situ* conductance measurements show that oligomeric films of Ind_2T_6 present the best stability and electrochromic switching performance. Enantioselective tests with a chiral ferrocene amine clearly show the potential as chiral selectors for analytical and sensing purposes.

1. Introduction

Since the discovery of conducting properties of polyacetylene in 1977,[1] great progress has been made researching on organic semiconductors (OSCs); in particular, polyaromatic structures were demonstrated to be very performant in terms of stability, charge transfer and optoelectronic properties.[2] Among them, thiophene based polymers and their boundless modifications have great interest for electroactive organic film preparation.[3–5] Notable examples are poly(3,4-ethylenedioxythiophene) (PEDOT) and poly(3-hexylthiophene) (P3HT) which are commercially available on a large scale[6–10] and employed in various optoelectronics and energy storage applications.[10,11]

The possibility to introduce chirality as peculiar feature in polythiophene-based organic semiconductors is a very recent research topic.[12] Many of these materials constitute fundamental tools in fabrication of active layers for chiral electrochemical sensing applications.[13] Investigations on polythiophenes led some of us to introduce 2,2′-bis(2,2′-bithiophene-5-yl)-3,3′-bithianaphthene (BT_2T_4, Scheme 1) as non-planar sexithiophene based monomer to obtain 3D electroactive oligothiophenes employed successfully as an effective crosslinker and 3D electropolymerization promoter.[14] Noteworthy, BT_2T_4 is a C_2 symmetric chiral molecule characterized by the presence of a stereogenic axis connecting the two benzothiophene subunits. Thus, the whole conjugated backbone is concurrently the source of both chirality and key functional properties which are reciprocally linked. On account of this coincidence, BT_2T_4 and structurally related analogues[14–16] were defined as "inherently chiral" compounds.[13] The oligothiophenes, resulting from their electro-oxidation, are endowed with greater chirality manifestations with respect to the traditional ones in which the stereogenic element is external to the conjugated backbone.[17] Oligothiophenes based on a biheteroaromatic scaffold can be electro-oxidized with activation of the two homotopic thienyl terminals generating higher order oligomers directly deposited on the electrode surface which can further be used as an electroactive layer.[17,18] Enantiopure films were extensively investigated as chiral electrochemical selectors showing high enantioselectivity towards the antipodes of different chiral probes.[17,19–21]

Recently, a new inherently chiral monomer based on 2,2′-biindole scaffold, namely the 3,3′-bis(2,2′-bithiophen-5-yl)-1,1′-dimethyl-1*H*,1′*H*-2,2′-biindole, nicknamed as $(N\text{-Me–Ind})_2T_4$ (Scheme 1), was synthesised as racemate and resolved into antipodes through enantioselective HPLC. The enantiopure films showed even higher enantioselection ability compared to BT_2T_4 analogues towards the enantiomers of different chiral probes.[22] In addition, $(N\text{-Me–Ind})_2T_4$ oligomeric enantiopure electroactive surfaces exhibited outstanding enantiodiscrimination even towards circularly polarized light components and electron spins, opening possible applications in chiroptics and spintronics fields. The atropoisomeric core, responsible for the important chiroptical and enantioselection manifestations of these systems, is also a defining element for their electro-

[a] C. Malacrida,[+] Dr. L. Scapinello,[+] Prof. S. Ludwigs
IPOC-Functional Polymers, Institute of Polymer Chemistry
University of Stuttgart
Pfaffenwaldring 55, 70569 Stuttgart, Germany
E-mail: sabine.ludwigs@ipoc.uni-stuttgart.de
[b] Dr. L. Scapinello,[+] Prof. A. Penoni, Prof. T. Benincori
Dipartimento di Scienza e Alta Tecnologia
Università degli Studi dell'Insubria
Via Valleggio 11, 22100 Como, Italy
E-mail: tiziana.benincori@uninsubria.it
[c] Dr. R. Cirilli
Centro Nazionale per il Controllo e la Valutazione dei Farmaci
Istituto Superiore di Sanità
Viale Regina Elena 299, 00161 Roma, Italy
[d] S. Grecchi
Dipartimento di Chimica
Università degli Studi di Milano
Via Golgi 19, 20133 Milano, Italy
[+] These authors contributed equally to this work

Supporting information for this article is available on the WWW under https://doi.org/10.1002/celc.202100511

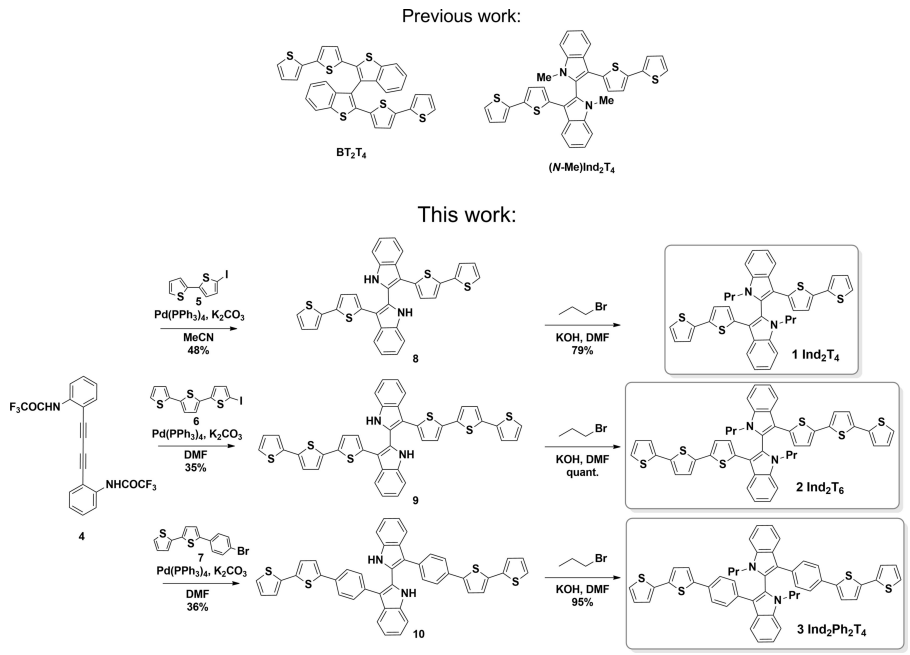

Scheme 1. BT_2T_4 and (N–Me)Ind_2T_4 (top); synthetic route to molecules 1 (Ind_2T_4), 2 ($Ind_2Ph_2T_4$) and 3 (Ind_2T_6) in their racemic forms (bottom).

chemical behavior. The partial conjugation between the two indole moieties through the interannular bond, as well as the interactions through space (for example between opposite oligothienyl-units in macrocycles), make the symmetric oligothienyl units acting as partially interacting equivalent redox moieties.[23,24]

In this manuscript, we introduce three new inherently chiral 2,2′-biindole monomers **1–3**, nicknamed as Ind_2T_4, Ind_2T_6 and $Ind_2Ph_2T_4$, functionalised in the 3,3′-positions with bithiophene (T_2), terthiophene (T_3), and phenylbithiophene (PhT_2) groups, respectively (Scheme 1). The nitrogen atoms of all compounds were alkylated with a propyl group to achieve good monomer solubility and oligomer processability.

A systematic electrochemical analysis of the monomers **1** (Ind_2T_4), **2** (Ind_2T_6) and **3** ($Ind_2Ph_2T_4$) and of the corresponding electro-oligomerized redox-active films oligo-**1** (oligo–Ind_2T_4), oligo-**2** (oligo–Ind_2T_6) and oligo-**3** (oligo–$Ind_2Ph_2T_4$) was carried out. *In-situ* spectroelectrochemistry was performed to analyze the electrochromic behavior and to help identifying the nature of the charged-states generated upon oxidation. Especially oligo-**2** showed remarkable properties with good switching abilities and a mixed-valence behavior upon oxidation of the oligothiophene units. The analysis and understanding of the charging properties and stability of 2,2′-biindoles-3,3′diheteroaryl electroactive films is important in view of their employment as chiral electrodes in enantiodiscrimination tests. The suitability of enantiopure oligo-**2** films as selectors for benchmark ferrocene probe is demonstrated and shows the potential of the electrochemically generated films for analytics and sensing applications.

2. Results and Discussion

2.1. Synthesis

The synthetic approach to 3,3′-diheteroaryl-2,2′-biindoles (Scheme 1) is inspired from work published by Arcadi et al.[25] in 2006. The reaction protocol uses a Pd catalysed double indole ring closure with 3,3′ functionalization just in a single step starting from trifluoroacetamide **4** and appropriate heteroaryl halide in refluxing acetonitrile (MeCN). The reaction of **4** with iodobithiophene **5** to synthesize biindole **8** was already presented.[22] Compounds **9** and **10** were respectively obtained from halides **6** and **7**. Solvent switching to refluxing DMF was used to afford biindoles **9** and **10** in discrete yield due to low solubility of starting halides **6** and **7**. The subsequent propylation step affords soluble and processable compounds **1–3** as racemates. Detailed synthesis protocols of all compounds are given in the Supporting Information.

The racemate of monomer **2** was resolved into antipodes by enantioselective HPLC on a polysaccharide based chiral stationary phase under normal phase mode. However, absolute configurations were not assigned: we generically refer to (*EN1*)-**2** as the first eluted enantiomer and (*EN2*)-**2** as the second eluted one.

The absorption spectra of compounds **1**, **2** and **3** are reported in Figure 1. The characteristic maximum wavelengths λ_{max} and extinction coefficients ε are reported in Table 1. All compounds show a maximum around 220 nm and another band at ~400 nm, and both can be attributed to π-π* transitions.[26] The absorption spectra of compounds **1** and **3** appear very similar in shape with only small variations of the absorption maximum λ_{max} at ~400 nm. In general, the λ_{max} are comparable with tabulated literature values for π-π* transitions

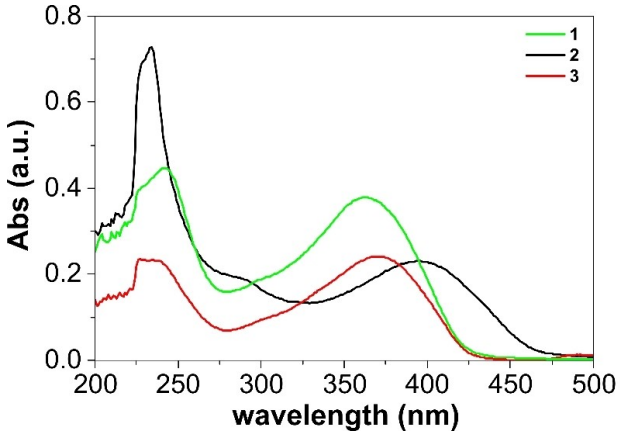

Figure 1. UV-Vis absorption solution spectra (CH_2Cl_2) of 1 (green curve), 2 (black curve) and 3 (red curve).

Table 1. Summary of absorption measurements and oxidation E_p from DPV experiments; analyte concentration 0.5 mM in CH_2Cl_2/NBu_4PF_6 0.1 M on ITO electrode; scan-rate 20 mV/s, voltage amplitude (ΔE) of 25 mV. $E^{\ominus} = Ep - \frac{\Delta E}{2}$ for reversible peaks.

Molecule	λ_{max} [nm]	ε_{max} [$L \cdot mol^{-1} \cdot cm^{-1}$]	E_p from DPV [V *vs* Fc/Fc^+]			
			A	B	C	D
1	364	44286	0.40	0.61	0.84	0.99
2	395	17958	0.33	0.53	0.70	0.85
3	373	36400	0.56	0.65	0.85	–

of bithiophene and terthiophene units.[27] More precisely, the observed transitions seem to result from intra-molecular charge transfer transitions (ICT) from the π system of the pyrrole ring of the core to the π* of the oligothiophene terminals, as evidenced by DFT calculations.[22] Considering the increase of the thienyl arms from two to three, a red shift of 31 nm with increase of the conjugation from **1** to **2** is observed. The introduction of the phenyl spacer induces a small increase of the absorption maximum of only 9 nm in comparison to the addition of a terthiophene unit. This is regarded as consequence of a less efficient conjugation of the phenyl unit.[28]

2.2. Electrochemical Characterization of the Monomers and Electrodeposition

The electrochemical characterization of **1**, **2** and **3** is presented in Figure 2. All the electrochemical analysis presented in the following section is performed on the monomers as well as on the oligomers in their racemate form. For all three molecules the oxidative cyclic voltammetry (CV) patterns are characterized by multiple peaks. Considering the structural differences between the molecules, a first couple of peaks (A, B) is observed for the first oxidation. Supported by previous calculations,[22] and because no oligomerization is possible by oxidation around this first set of peaks (Figure 2a, c, e), the oxidations associated with these two signals (A, B) should be localized on the more electron-rich indole moieties with only partial delocalization on the oligo–thiophene system. That suggests that the two peaks belong to the two interacting radical cations which are localized on both indole centers, *i.e.* two $IndT_2$, $IndPhT_2$ and $IndT_3$ partially interacting redox sites. In Scheme 2, the oxidation steps of 2 are reported as an example.

A second couple of peaks (C, D) is obtained by polarizing the working electrode (WE) at more positive potentials which can be attributed to the activation of the thienyl terminals. Indeed, oxidation at the levels of these two peaks in CH_2Cl_2 is followed by the electrodeposition of electroactive films upon multiple cycling (Figure 2b, d, f). The coupling of the so

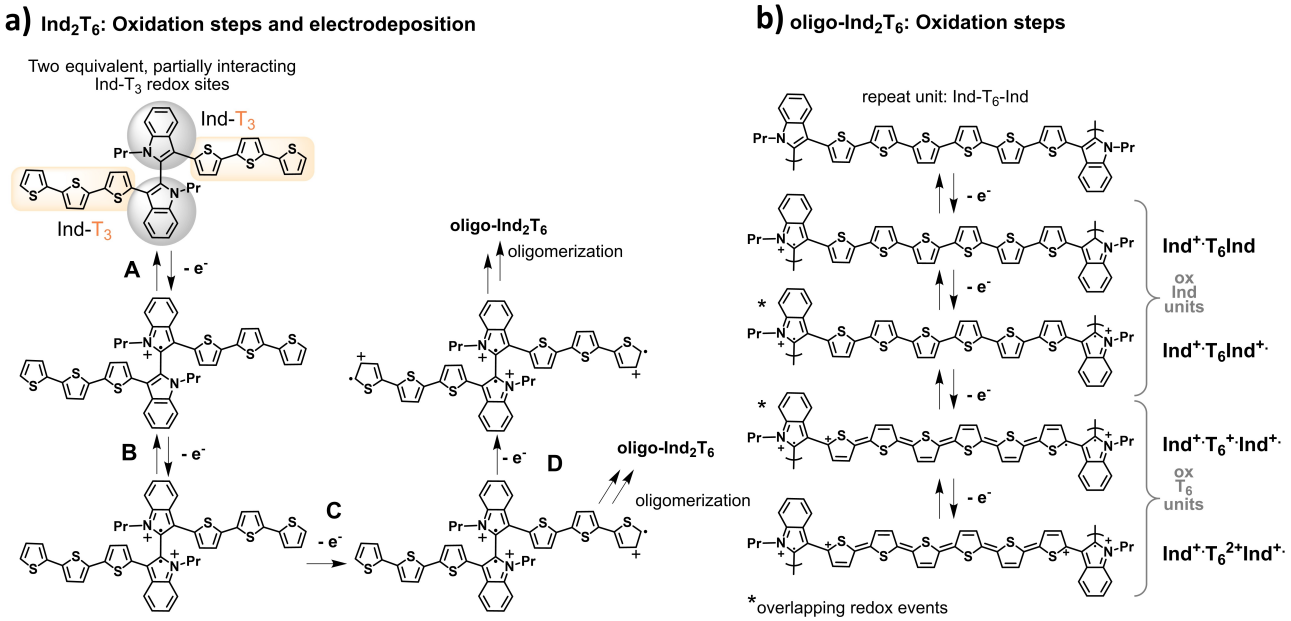

Scheme 2. Exemplification of the oxidation scheme for compound 2 (Ind_2T_6) leading to electrodeposition of oligo-2, with reference to Figure 2.

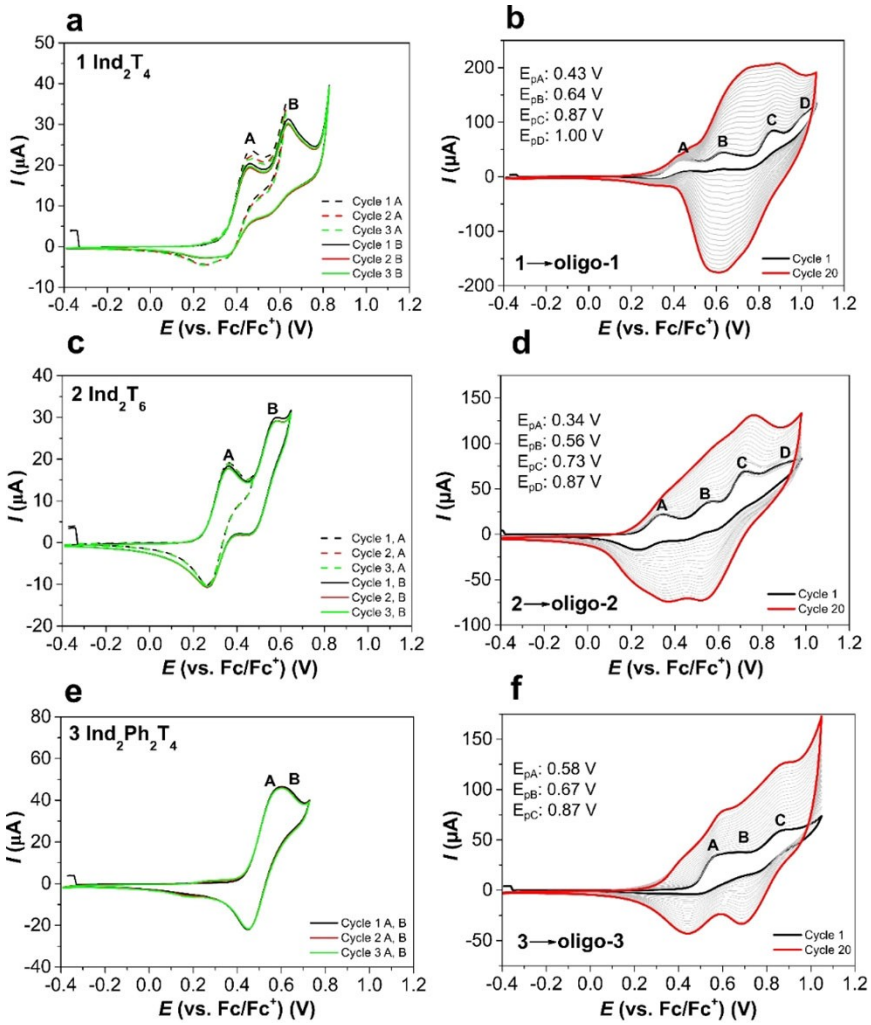

Figure 2. Cyclic voltammetry of molecules a) 1, c) 2 and e) 3 in CH_2Cl_2/NBu_4PF_6 0.1 M at a scan-rate of 20 mV/s; multiple cycles around the first (A) and second (B) peaks of oxidation are shown. Electrodeposition of b) 1, d) 2 and f) 3 by multiple cycling around the III (C) and IV (D) oxidation peaks at a scan-rate of 20 mV/s and a monomer concentration of 0.5 mM; ITO electrode.

generated radical cations at the free α thienyl positions generates oligomers of higher order which nucleate on the electrode surface. Differential Pulse Voltammetry (DPV) experiments also clearly show four peaks with E_{pA} and E_{pB} corresponding to the symmetric double-radical cation oxidation centered mainly on the indole core, and E_{pC} and E_{pD} corresponding to the oxidation involving the reactive thiophene alpha terminals, Figure S1.

Table 1 collects the peak potentials (E_p) from the DPV experiments (Figure S1 supporting information) of all analyzed compounds. The CV and DPV measurements registered for compounds **1** and **2** present strong similarities with each other. The first couple of peaks A and B shows for both molecules a similar peak-to-peak potential separation $\Delta E_{pB\text{-}pA}$ of 22 mV. For compound **1** $E_{pA}(\mathbf{1}) = 0.44$ V and $E_{pB}(\mathbf{1}) = 0.62$ V and for compound **2** $E_{pA}(\mathbf{2}) = 0.33$ V and $E_{pB}(2) = 0.55$ V are measured.

In the case of the phenyl substituted molecule **3**, this separation is significantly lower with $\Delta E_{pB\text{-}pA}$ around 10 mV, with $E_{pA}(3) = 0.56$ V and $E_{pB}(3) = 0.65$ V, and shifted towards more positive potentials, compared to the second oxidation peak of **1**. Further, in the case of compound **3** the fourth oxidation peak (D) is not observed from the CV experiments as for compounds **1** and **2**.

For a higher conjugation efficiency between equivalent redox centers, a higher peak potential separation is expected. An explanation to the smaller separation of peaks A and B of compound **3** could be ascribed to a slightly higher torsion between the two moieties resulting from the presence of a phenyl group, more sterically hindered in comparison to the thiophene units. In these atropoisomeric systems indeed, the conjugation efficiency is inversely proportional to the torsional angle.[17,22] Further, the results might also be explained by the higher degree of aromaticity of the phenyl linker, which makes it a less efficient π-spacer in comparison to the thiophene unit.[28,29] The structural similarity of **1** and **2** with the good correlation in their peak-to-peak separation suggests overall a similar degree of interaction between the two symmetric moieties in accordance with their similar structures.

The lower oxidation potential for all oxidations of compound **2**, with respect to **1** and **3**, correlates further well with the higher conjugation of the T_3 in comparison to the T_2 and PhT_2 units.

The peak-to-peak separation encountered for the second couple of peaks (C, D) of oxidation is overall lower than in the case of the oxidation at the biindole core (A, B). In a previous work, it was found that peak splitting is strongly dependent on solvent polarity. In particular, the use of a solvent such as acetonitrile having a higher dipolar moment than CH_2Cl_2 results in the twin peak merging. Further, the charge screening ability and stabilization of the oxidation products in CH_3CN does not lead to electrodeposition.[22,30] Examples of solvent influence on the radical-cation reactivity towards dimerization can be found in the literature.[22,31]

As mentioned above, potentiodynamic cycling around the peaks associated with activation of the thienyl alpha terminals of the molecules, *i.e.* peaks C and D, results in electrodeposition of oligomers. Examples of electrodeposition of compounds **1**, **2** and **3** performed in racemate monomer solutions by subsequent potentiodynamic cycles are presented in Figure 2. The film growth appears for all the species rather regular with a reversible CV pattern also for a higher number of cycles. In all cases, upon potentiodynamic oxidation some of the oxidized monomers were observed to diffuse away from the electrode surface. After electrodeposition, the samples were carefully rinsed with dichloromethane to remove excess of monomer and electrolyte, dried and stored in inert atmosphere.[32]

Due to the presence of the atropoisomeric scaffold, the effective conjugation length between the two symmetric units of the molecule is limited. The electroactive film can be therefore regarded as constituted by a series of "localized" redox units (Scheme 2).[33] A direct determination of the film composition by MALDI was not possible as the films are obtained in a partially charged state. Considering the structural similarities with (*N*-Me–Ind)$_2$T$_4$,[22] we expect that the herein electrodeposited films are constituted by a series of oligomers with the same conjugation length, namely oligo-**1**, oligo-**2** and oligo-**3**, in the form of open and closed oligomers.[17,22] In particular, a similar outcome was obtained after chemical oxidation with $FeCl_3$ in $CHCl_3$ of (*N*-Me–Ind)$_2$T$_4$, from which it was possible to isolate in a pure state the closed dimer.[22] The specific composition of each film might depend on the deposition conditions including scan-rate, monomer concentration or substrate nature. Similar cyclic structures can be found upon oxidation of other inherently chiral monomers.[15,18,22]

2.3. Electrochemical Characterization of Electro-oligomerized Films

Both standard cyclic voltammetry on Au and *in-situ* spectroelectrochemistry on ITO were performed on the electrodeposited oligo–indole films in monomer free solution. CVs are presented in Figure 3 and Figure S2. Similar CV patterns are registered for the different electrodes. The characteristic half-wave potentials $E^{1/2}$ for the different compounds are listed in Table 2. In the case of oligo-**1** multiple overlapped oxidation waves with half wave potentials $E^{1/2}$ of 0.18 V, 0.53 V and 0.73 V are measured. The CV of oligo-**2** presents three oxidation waves with $E^{1/2}$ at 0.20 V, 0.39 V and 0.58 V. Two reversible oxidation waves with $E^{1/2}$ of 0.43 V and 0.71 V are visible for oligo-**3**.

The electroactive films were subjected to multiple oxidative cycles (100 cycles at a scan-rate of 200 mV/s) showing good stability after several charge/discharge processes (Figure S3). A scan-rate analysis of the oligomer films (Figure S4) deposited on Au shows that the anodic and cathodic peak currents (I_p) follow a linear trend up to scan-rates of $v < 500\ mV\,s^{-1}$ in the case of oligo-**2** and oligo-**3**. For higher scan-rates diffusion limitations are encountered. Interestingly, in the case of oligo-**1** films a peak-current to scan-rate linearity is valid only for $v < 300\ mV\,s^{-1}$. The lower conjugation length of oligo-**1** could explain this experimental observation.

An *in situ* UV-Vis-NIR spectroelectrochemical characterization of the electrodeposited film was performed with the aim to elucidate the nature of the charged species. In Figure 3b, d and f characteristic spectra taken during oxidation are highlighted. To monitor the relative distribution of the different states of charge, neutral (N), radical cation ($R^{+\bullet}$) and dication (D^{2+}) states of the films, the absorption at selected wavelengths was plotted as function of the electrode potential in Figure 3a, c and e in superposition with the CV. Absorbances at specific wavelengths can be correlated to the concentration of the different states of charge considering different extinction coefficients for different wavelengths.[34] These results are further combined with *in-situ* conductance measurements allowing for a more detailed assignment of the states of charge, and to analyze the conductive properties of these materials.

Oligo–Ind$_2$T$_4$ (oligo-1): The electrodeposited films of oligo-**1** present in the neutral state (N) a strong band with a maximum at 425 nm, Figure 3b. Furthermore, two less pronounced bands at 673 nm and 1151 nm are visible. Upon increasing the oxidation potential, the intensity of the neutral band decreases with concurrent increase of the bands at 673 nm and 1151 nm. The band at 1151 nm evolves in two maxima (orange to green spectra Figure 3b) at 1295 nm and 999 nm upon progressive increase of the oxidation potential. For potential values more positive than +0.61 V a peak at 552 nm is formed gaining in intensity with increasing oxidation potential. The initial absorption is reversibly recovered during the discharging cycle (supporting information Figure S5). The redox discharge-ability was further analyzed by chronoamperometry (Figure S8), from which a reversible charge/discharge

Table 2. Characteristic wavelengths for different states of charge from spectroelectrochemical experiments.

	λ_{max} [nm]		
	N	$R^{+\bullet}$	D^{2+}
oligo-**1**	425	673, 1151	552, 999 1295
oligo-**2**	452	713; (826)	556; (902); 1278
oligo-**3**	412	606; 743	546; (929); 1227

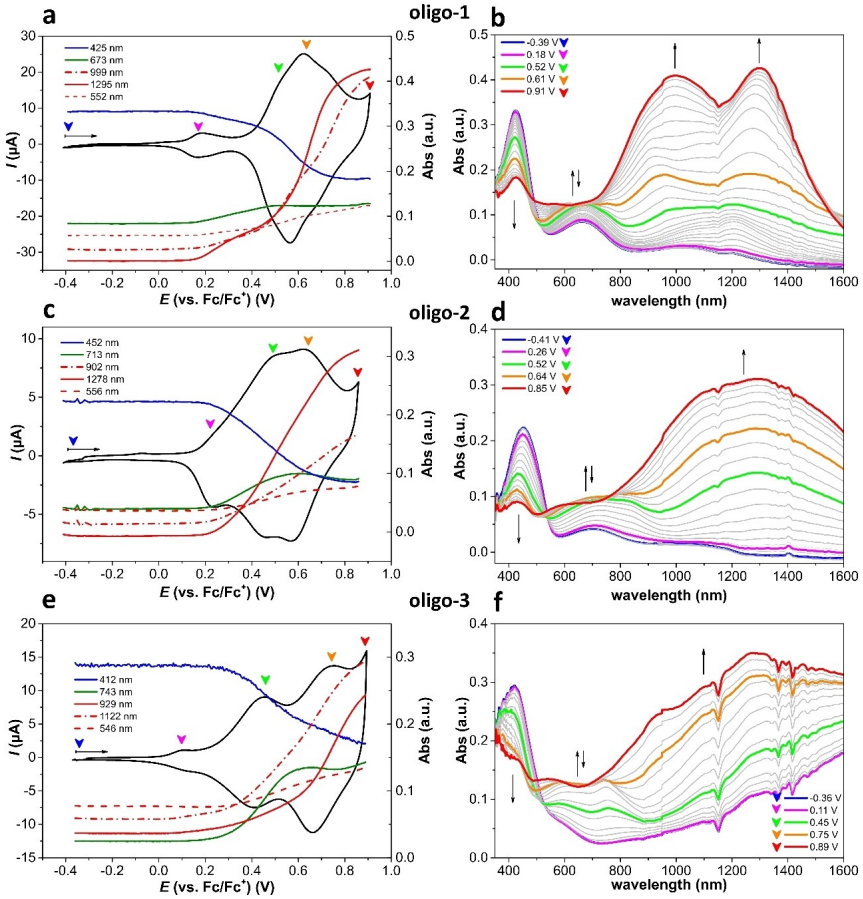

Figure 3. UV-Vis-NIR spectroelectrochemical measurements registered during the forward oxidation cycle at a scan-rate of 20 mVs^{-1} in 0.1 M CH_2Cl_2/NBu_4PF_6. Left side: CVs and peak-trends of characteristic absorption wavelengths; right side: corresponding UV-Vis-NIR spectra registered for oligo-**1** (a, b); oligo-**2** (c, d) and oligo-**3** (e, f).

process with only minimal loss of the neutral absorption (T% at 425 nm) upon 10 subsequent charge/discharge cycles is observed.

The peak-trend as function of the potential for the charging of oligo-**1** is presented in Figure 3a. The blue curve represents the peak absorption variation for the neutral state (425 nm), the green curve for the first oxidized radical cation state (673 nm), and the red curves for the dication state (552, 999 and 1295 nm). The potential dependent peak-absorption is characterized by a step-like variation of the absorbances for the neutral (blue line) and oxidized state (red and green lines) which correlate well with the redox peaks in the CV experiment. A first (small) change of absorption is observed concurrently with the first absorption peak with an onset for the absorption variation at 0.15 V, coinciding with the electrochemical onset. For potentials more positive than 0.4 V the neutral band starts to decrease in intensity significantly. This is followed by the band at 673 nm reaching an intensity maximum at 0.49 V, the value corresponding to the second redox peak observed in the voltammogram. For potential values more positive than 0.4 V also the bands in the NIR at 999 and 1295 nm are characterized by a marked intensity variation.

In the case of oligo-**1** the intensity of the band for the π-π* transition in the neutral state (425 nm) is associated with significant changes in absorption at a potential value more positive than +0.4 V *vs* $Fc^+|Fc$, some hundreds of mV after the oxidation onset and the first redox peak (0.23 V). A possible explanation could be that the first oxidation is ($N/R^{+\bullet}$) localized on a moiety of the biindole core, causing only a limited planarization of the structure. Significant variations of the absorption properties are obtained only by further charging, as the oxidation of the thiophene chains is addressed and the structure passing from aromatic to quinoid.[18] Moreover, it should also be considered that indole absorption is located at higher energies with respect to a tetrathiophene system. The spectrum seems to change only when the second, interacting indole moiety and the thiophene chain are oxidized.

Oligo–$Ind_2Ph_2T_4$ (oligo-3)*:* Figure 3e, f shows the analysis of oligo-**3** (complete data Figure S7). In the neutral state, the film is characterized by an absorption maximum at 412 nm, Figure 3f. Upon increase of the oxidation potential the neutral band (412 nm) bleaches with concurrent formation of two bands at 743 nm and 1122 nm, which are assigned to the radical cation state localized on the Ph–T_4–Ph units. Upon further increase of the oxidation potential during the forward

scan, the band at 743 nm reaches its maximum of absorption at a potential value of 0.62 V. In correspondence with the third redox wave, the film absorption further changes, showing a broadening of the low-energy band also in the spectral region of 800–1000 nm (a wavelength of 929 nm is sampled for peak-trend).

The peak-trend as function of the potential is analyzed in Figure 3e. The first redox signal observed for oligo-**3** consists of a small reversible couple of peaks at $E^{1/2}$ 0.14 V. Interestingly, no absorption variations were observed in the range of potentials of this peak. Significant variations in the absorption pattern are observed only at potentials more positive than 0.23 V. This potential value should be assigned, in the forward scan, to the concomitant oxidation localized on the biindole core, and the oxidation on the Ph–T_4–Ph moieties at the radical cation level. The absorption at 743 nm, green line, increases up to 0.62 V during the forward scan of oxidation, this value well matches the simultaneous oxidation of the indole centers and the Ph–T_4–Ph units to their radical cation state at $E^{1/2}$ 0.47 V. The potential value 0.62 V also coincides for the forward scan of oxidation with the abrupt increase in absorption of the band at 929 nm during the redox event and is associated with the oxidation of Ph–T_4–Ph units to the dication level. Oligo-**3** can be charged/discharged repeated times reversibly with complete recovery of the absorption of the neutral state (Figure S10).

Oligo–Ind$_2$T$_6$ (oligo-2): *In situ* UV-Vis-NIR spectroelectrochemistry of electrodeposited oligo-**2** film (Figure 3c, d and Figure S6) is characterized by an absorption maximum in the neutral state (blue curve) of 452 nm. Upon polarization to values more positive than 0.14 V, which coincides with the electrochemical onset, the neutral band (452 nm) progressively bleaches with concurrent formation and increase in intensity of two bands at 713 nm (green-line) and 1278 nm (red-line). These bands are assigned to the radical-cation and dication state localized on the T_6 moieties of oligo-**2**, respectively. The middle-energy band with a maximum at 713 nm reaches an absorption maximum during the forward oxidation scan at ca. 0.6 V, between the second and third couple of redox waves found in the CV signal. Upon potential values superior to 0.52 V (second redox wave, orange band in the spectra) the band with a maximum at 1278 nm broadens, showing absorption also in the spectral region of 750–1000 nm (λ 902 nm was sampled, red dashed line) and at 556 nm. Oligo-**2** can be reversibly oxidized over several cycles, without loss of absorption properties.

Comparing the three oligomer films, they are all characterized in the neutral state after deposition by similar patterns of absorption. The λ_{max} in the case of oligo-**2**, which is characterized by the highest conjugation length, is found at 452 nm; in the case of oligo-**1** at 425 nm and of oligo-**3** at 412 nm. Generally, a red shift from the monomer absorption is found upon electrodeposition due to the increased conjugation. The absorption maxima in the neutral state of oligo-**1** and oligo-**3** find good correlation with the one measured in CH_2Cl_2 for the π-π * transition of T_4 oligomers (408 nm), and of oligo-**2** with the maxima of T_6 (449 nm).[35] In general this correlation is also observed for the different states of charge, indicating that the biindole central core has a limited effect on the spectroscopic properties of the molecules. Interestingly, the introduction of the phenyl spacers presents an absorption maximum at lower wavelengths in oligo-**3**, with respect to oligo-**1**, despite the higher amounts of conjugated units. This experimental observation could result from the higher steric hindrance introduced by the phenyl units limiting planarity and causing a loss in the conjugation efficiency. As already observed from the monomer analysis, the introduction of the phenyl unit as spacer reduces the conjugation efficiency both at the level of the atropoisomeric core, and at the level of the oligothienyl units (increasing the distortion of the conjugated backbone) resulting in an increase of the ionization potential.[28,36] As consequence of the increase in conjugation length after oligomerization, the oxidation of the oligo–thiophene units of the electrodeposition products takes place with completely or partial superimposition to the biindole core oxidation. Analogously, the oxidation localized on the indole core shifts towards less positive potentials with respect to the monomers. The charging steps of oligo-**2** are proposed in Scheme 2 b, similar oxidation steps are expected for the other oligomers.

The onset of oxidation in the case of oligo-**1** and oligo-**2** is defined by the redox-activity of the biindolic core. In the case of oligo-**1**, an almost baseline separated peak is measured at 0.23 V, which is 17 mV shifted to lower potentials in comparison to the biindole oxidation in the associated monomer. The hexathiophene oxidation at the radical cation level of oligo-**2** is almost completely superimposed to the oxidation centered on the biindole, for which only a shoulder at 0.20 V is measured. For oligo-**3** the radical cation oxidation of the tetrathiophenes is almost completely superimposed to the biindole centered oxidation, evidenced by spectroelectrochemistry data.[30,37]

It has to be mentioned that all the samples as obtained after electrodeposition are already characterized by two shoulders at ca. 700 and 1100 nm, wavelength regions which are characteristic for the radical cation state as observed from the potential dependent spectra. This result hints to a partial oxidation of the films after electrodeposition. The same shoulder remains present, without change in intensity, also upon pre-polarization at negative potentials. Studies on electropolymerization of indole by Inzelt et al.[38] revealed that during the electrodeposition a fraction of the polymer and of the monomers are overoxidized leading to non-uniform film deposition. Further, the authors found that even traces of oxygen in the solution containing the monomer could lead to the oxidation of the monomer and electropolymerization.

2.3.1. Electrochromism and Mixed Valence States

All electrodeposited films present similar signature in the different states of charge, in particular, the fully oxidized state (red curve) presents a characteristic peak at ca 550 nm and around 1200 nm in the NIR region, Figure 3. The electrodeposited films also show good electrochromic properties with a fast and reversible switch between neutral and oxidized state as evidenced by the chrono-charge-discharge experiments presented in Figure S8–10. Interestingly, a very good correlation

with similar ΔT% and switching times is found between oligo-**1** and oligo-**2** which might also correlate to their structural similarities. Upon switching between neutral and fully oxidised state, a ΔT% of 18% and 22% are measured for the absorption maxima characteristic for the neutral state, and a ΔT% of 56% and 53% for the NIR absorption maximum are measured for oligo-**1** and oligo-**2**, respectively. The colour change together with the transmittance behavior of oligo-**2** are given in Figure 4a, clearly showing transparency for the neutral and oxidized states. In the case of oligo-**3**, a ΔT% of 15% for the neutral maximum and a ΔT% of 35% for the NIR maximum are measured. For the complete data set we refer to Figure S8–10 in the Supporting Information.

To get further information on the conductivity behavior *in-situ* conductance measurements were performed using interdigitated electrodes (IDE) on which the films were electrodeposited. The successful coverage of the interdigitated area after electrooligomerization was assured by scanning electron microscopy (SEM). Scanning electron microscopy on electrodeposited samples on IDE electrodes (Figure S11, supporting Information) shows rather homogeneous surface deposits with a complete coverage of the whole interdigitated area. The samples are characterized by film thickness between 200–300 nm, determined by Atomic Force Microscopy by measuring next to scratches.

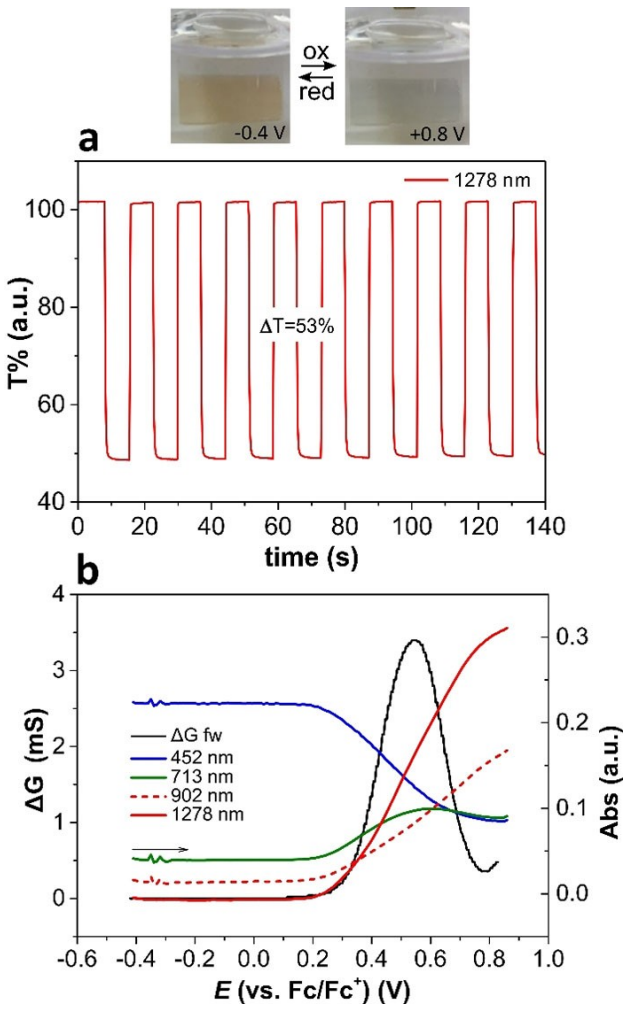

Figure 4. oligo-2: a) Pictures of an oligo-2 film in neutral and fully oxidised state together with electrochromic switching between −0.4 V and 0.8 V (T% sampled at 1278 nm). b) *In-situ* conductance forward cycle oxidation (black curve) overimposed to absorption peak-trends registered for the forward oxidation; measurements registered with a scan-rate of 20 mVs^{-1} in 0.1 M CH_2Cl_2/NBu_4PF_6.

In-situ conductance of electrodeposited oligo-**2** is presented in Figure 4b and Figure S12; in the case of oligo-**1** and oligo-**3** the drain currents from which *in-situ* conductance is measured were too low to be distinguished from the background current. The conductance onset of oligo-**2** is found in correspondence with the electrochemical onset. The main conductance maximum is localized at 0.55 V for the forward scan and 0.50 V in the backward scan of the CV cycle, in proximity of the half-wave potential for the $R^{+\bullet}/D^{2+}$ oxidation of the hexathiophene units. Further, a small conductance peak can be distinguished for the backward scan at ca. 0.20 V, in correspondence to the oxidation of biindole cores. Upon these observations, the *in-situ* conductance behavior of oligo-**2** can also be described in terms of mixed valence conductivity. In the neutral state as well as for the dication state the films is characterized by a low conductance, whereas for potential values corresponding to the concurrent presence of radical cation and dication species localized on the T_6 units ($Ind^{+\bullet}T_6{}^{+\bullet}Ind^{+\bullet}/Ind^{+\bullet}T_6{}^{2+}Ind^{+\bullet}$), the highest conductance is registered. *In-situ* conductance analysis of oligo-**2** evidences a mixed valence conductivity behavior, with the highest conductance change observed for the redox couple $R^{+\bullet}/D^{2+}$ species involving higher delocalization over the T_6 units ($Ind^{+\bullet}T_6{}^{+\bullet}Ind^{+\bullet}/Ind^{+\bullet}T_6{}^{2+}Ind^{+\bullet}$). Several overlapping redox states have to be considered: open and closed oligomers with slightly different $E^{1/2}$ causing a broadening of the conductance window in comparison to pure redox systems. The conductance change is associated with the oxidation involving the oligo–thienyl units as the redox change $N/R^{+\bullet}$ more localized on the biindolic center ($(Ind^{+\bullet}T_6Ind/Ind^{+\bullet}T_6{}^{2+}Ind^{+\bullet})$, first peak) is characterized only by a small change in conductance in comparison to T_6, observable during the discharge cycle. This might be explained by the fact that the indole-centers are highly spatially separated resulting in an inefficient center distribution for electron hopping. Overall, the conductance behavior observed seems to follow the findings from Zotti et al..[39,40] The results also well correlate the peak-trend variation for the different redox states of the film, which find for hexathiophene units conductance sustained by a hopping mechanism between radical-cation and dication states.[39–41] The introduction of indole redox centers does not modify this type of behavior. The experimental results are also in accordance with previous studies on oligo–BT_2T_4 and oligo–BT_2E_4.[14,15] The *in-situ* conductance plot is reversible within different cycles; the conductance values are lower during the reverse scan in comparison to the forward scan and hysteresis phenomena are also observed. One possible explanation for the lower conductance values measured during the backward scan in comparison to the forward oxidation sweep could be, as proposed by Ofer et al.,[42] the overcoming of a kinetic barrier during the oxidation process. The authors

suggest that as the polymer becomes highly oxidized, coulombic repulsions might lead to changes in chain conformations, in order to stabilize the progressively more localized charges. The conformation adopted to diminish coulombic repulsions is non-optimal for conductivity, consequently the conductivity curve during the backward scan could present lower conductance values. This asymmetry between conductivity in the forward and backward scan can be observed in various systems in the literature.[30,43,44] Observation of hysteresis during *in-situ* measurements in conducting polymers is a very common phenomenon. Several explanations have been proposed including: incomplete reversibility of the redox process, stabilization of the charged state or structural change in the charged state with formation of σ-dimers.[45,46] Further film thickness and diffusion of ions during the charge/discharge process also play a significant role in determining the extent of hysteresis.[45,47]

Overall, the substitution of the dibenzothiophene with biindolic moieties does not induce significant variations in the absorption properties of the electrodeposited film concerning the position and topology of the bands, similarly the conductivity properties of this class of molecules remain dominated by the ones of the oligothienyl moieties.

2.3.2. Enantioselection Tests

The enantioselection ability of oligo-**2** films prepared by the electrooligomerization of the corresponding enantiopure monomers (*EN1*)-**2** and (*EN2*)-**2** was further tested. Enantiodiscrimination experiments were performed by Differential Pulse Voltammetry (DPV, 5 mV step, 50 mV amplitude) using 0.002 M solutions of the chiral probes ((*S*)-(−)- or (*R*)-(+)-*N,N'*-dimethyl-1-ferrocenylethylamine) named (*R*)-Fc and (*S*)-Fc in 0.1 M CH_2Cl_2/NBu_4PF_6 as supporting electrolyte (Figure 5a, b).

These chiral probes are generally nice model compounds when testing new advanced chiral selectors, on account of ferrocene's facile and reversible electron transfer at a mild oxidation potential (in a region where the film is generally uncharged, *i.e.* in a potential range close to 0 V *vs* $Fc^+|Fc$), Figure S16. In the case of a bare GC electrode, upon oxidation of both enantiomers of the chiral ferrocenyl-probes, no variations in peak potential were observed (E_p: −0.09 V, grey curves). However, when changing to electrodes coated with enantiopure films of oligo-**2**, two splitted and quite different DPV signals, both well defined, are observed for the oxidation of (*R*)-Fc (green curves) and (*S*)-Fc (red curves).

A good enantiodiscrimination in terms of peak potential values is obtained, specularly for the two enantiopure films, with a separation of ~40 mV between the two antipodes (for oligo-(*EN2*)-**2** E_p of (*R*)-Fc: −0.040 V and (*S*)-Fc: −0.080 V) (Figure 5c, d). Reproducibility tests were performed by repeatedly recording the DPV patterns of model probes on freshly deposited chiral surfaces (dotted and dashed lines of (*R*)-Fc (green) and (*S*)-Fc DPV curves.

The electron-transfer process must take place at the interface between the metal electrode and the probe molecule

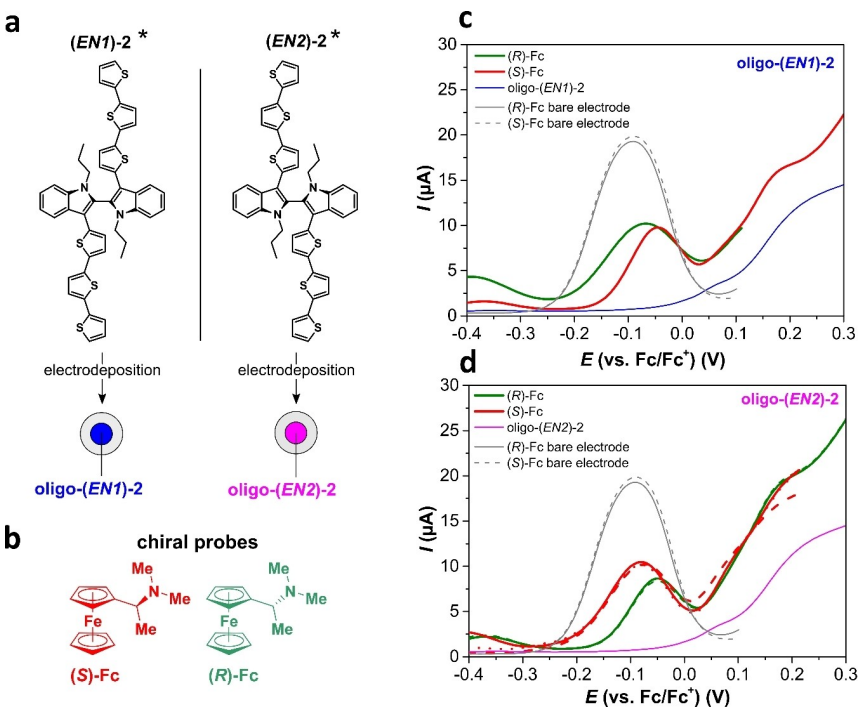

Figure 5. a) Sketch of enantiopure oligo-(*EN1*)-2 (c) and oligo-(*EN2*)-2 (d) deposited on GC electrode. (b) Electroactive ferrocenyl-probes employed: (*S*)-(−)- and (*R*)-(+)-*N, N'*-dimethyl-1-ferrocenylethylamine, named (*S*)-Fc (red) and (*R*)-Fc (green). c) and d) DPV measurements showing performances of enantiopure oligo-(*EN1*)-2 and of oligo-(*EN2*)-2 electrode surfaces towards chiral electroactive ferrocenyl-probes. In grey are also reported the signals of (*R*)-Fc and (*S*)-Fc recorded on bare GC electrodes. The blue line in c) corresponds to the DPV pattern of oligo-(*EN1*)-2 and the pink line in d) of oligo-(*EN2*)-2. Reproducibility tests on the two ferrocenyl-probes are also reported with dashed or dotted lines and the associated colour. *Enantiomers were resolved by chiral HPLC but no configuration was assigned: represented configurations might not correlate to the real ones.

within the chiral oligomeric film. The oxidation of chiral probes takes place at potential values at which the films are not yet oxidized. A possible explanation of the potential split could be that the interactions of the enantiopure probes with the enantiopure environment are of diastereomeric nature, and are therefore significantly affected by the energetics of the electron-transfer process in both thermodynamic and kinetic terms. For sake of comparison, Racemic-**2** (namely (±)-**2**) was also electrodeposited at constant working protocol, testing the enantiomers (*R*)-Fc and (*S*)-Fc. The results reported in Figure S15 (Supporting Information) confirmed that the potential shift is determined by the combination of the enantiopure chiral electrode surface with the chiral probe.

3. Conclusions

In this work the synthesis of three new inherently chiral molecules **1**, **2** and **3** was presented. The redox behavior of the molecules, which are endowed with symmetric oligothienyl terminals, linked through an internal indole core, is characteristic of interacting equivalent redox moieties. Comparing monomers **2** and **1**, we found that the introduction of an additional thienyl unit in **2** induces a shift to less positive potential values for the oxidation in comparison to **1** but identical peak-to-peak separations hinting to the fact that the two molecules have similar residual interactions. In the case of monomer **3**, characterized by a phenyl spacer, this separation is significantly lower; the results are explained by the less efficient conjugation of a phenyl unit in comparison to a thienyl unit. All molecules could be successfully electrodeposited; the resulting redox active films are stable upon oxidation. The electrochromic properties of the films are analyzed showing that all electroactive films can be repeatedly charged/discharged between their neutral and oxidised states in a highly reversible fashion.

Compared to earlier work on BT_2T_4 molecules, we found that the substitution of the 3,3′-bithianaphthene with a 2,2′-biindole scaffold does not induce significant variations in the absorption properties of the electrodeposited films concerning the position and topology of the bands at different states of charge, with absorption maxima well correlating with the one of the respective oligothienyl moieties. The analysis of *in-situ* conductance also hints to the fact that the biindole scaffold plays only a marginal role in determining charge transport within the system. The oligothienyl moieties behave as mixed-valence systems showing maximum conductance when both radical cation and dication state are present.[43,48] This is in agreement with earlier results from Zotti et al.[39,40]

The enantiodiscrimination ability of enantiopure oligo-**2** films was demonstrated with (*S*)-(−)- or (*R*)-(+)-*N*,*N*′-dimethyl-1-ferrocenylethylamine chiral probes. A peak potential separation of ~40 mV between the two antipodes was reproducibly measured, specularly for the two enantiomeric films. Future work will focus on the enantioselective performance of biindole films for analyzing more advanced and performant chiral probes for applications in analytic and sensing applications. Further, the reversible electrochromic behavior of these systems might trigger research on chiral electrochromic devices. In this context the synthesis of atropisomeric biindole low bandgap molecules endowed with electron-withdrawing groups in donor-acceptor architectures becomes also highly relevant for fine-tuning electrochromism.

Experimental Section

Electrochemical measurements were performed with an Autolab PGSTAT204 potentiostat (Metrohm Autolab, Utrecht, The Netherlands) at room temperature and under Argon atmosphere. A three-electrode glass cell provided with a Pt plate as counter electrode (CE) and an AgCl-coated silver wire as pseudo reference electrode (RE) were employed. As working electrode (WE) (a) ITO-coated glass slides S ~0.4 cm^2 ($\leq$20 Ω/sq, PGO, Germany) or (b) Au (vacuum deposited on glass slides over 3 nm of adhesion Cr layer; 30 nm Au layer) S ~0.5 cm^2 slides and (c) Pt interdigitated electrodes with a 10 μm band width were used. Prior to usage, the ITO electrodes were subjected to a 10 min treatment in a plasma chamber. For all the electrochemical measurements a 0.1 M CH_2Cl_2 solution (Sigma Aldrich, HPLC grade, dry) with Bu_4NPF_6 as supporting electrolyte (Sigma Aldrich, electrochemical grade) was employed as received. The electrolyte solution was degassed through Argon bubbling before the measurements. All potentials were referenced to the formal potential of the $Fc|Fc^+$ reference redox couple, measured in the same conditions of the analytes. Electrodeposition of racemate films was performed under potentiodynamic conditions on different electrode substrates (20 cycles at a scan rate of 20 $mV\,s^{-1}$; monomer concentration 0.5 mM in 0.1 M CH_2Cl_2/Bu_4NPF_6, specific modifications to the deposition conditions are otherwise noted). After electrodeposition, the films were washed with CH_2Cl_2 to remove residual Bu_4NPF_6 and monomers and the samples were stored under inert atmosphere.

Thin-film *in situ* spectroelectrochemical measurements were performed using an Autolab PGSTAT204 potentiostat (Metrohm Autolab, Utrecht, The Netherlands) and a Zeiss UV-vis spectrometer endowed with a MCS621 Vis II spectrometer cassette and a CLH600F lamp or a Zeiss UV-vis-NIR spectrometer endowed with a MCS621 Vis II and a MCS611 NIR 2.2 μ spectrometer cassette and a CLH600F lamp and using optical fibres (OceanInside). The measurements were conducted in a custom-made three-electrodes quartz cell employing a Pt wire as CE, an AgCl coated Ag wire as (pseudo) reference electrode and the coated ITO slides as WE. For spectroelectrochemical measurements the oligomeric films were electrodeposited on ITO substrates, surface area ~0.4 cm^2; 30 cycles, scan rate of 50 $mV\,s^{-1}$,0.5 mM monomer in 0.1 M CH_2Cl_2/Bu_4NPF_6)

The measurements were performed under Ar atmosphere and all the potential values were referenced to the formal potential of the $Fc|Fc^+$ redox couple. *In-situ* spectroelectrochemical measurements were conducted with a scan rate of 20 $mV\,s^{-1}$ and potential steps of 10 mV, with simultaneous recording of electrochemical data points and UV-Vis-NIR spectra.

***In situ* conductance experiments** combined to CV experiments were performed on Pt interdigitated working electrodes from DropSens (comb distance = 10 μm). The CV experiments were performed at room temperature under argon atmosphere using an Autolab PGSTAT204 potentiostat (Metrohm) with a Pt wire as CE and an AgCl-coated Ag wire directly immersed into the electrolyte solution as pseudoreference electrode. A constant bias (E_d) of 10 mV was applied between the combs of the interdigitated electrode using a second potentiostat (μStat400, DropSens) measuring the current (I_d) which is flowing between the two combs of

the interdigitated electrodes as a function of the potential in the CV measurement. With the help of two resistors (Heka interface), both current signals are separated to allow to conduct both the CV measurements and to measure the *in-situ* conductance simultaneously. The conductance value G was calculated from the measured current flowing between the combs according to Ohm's law $G = 1/R = I/V$. Electrolyte solutions (0.1 M Bu_4NPF_6/CH_3CN) were deaerated by argon bubbling before use. Conductance values are given as conductance change (ΔG) with respect to the conductance of the materials in the neutral state.

Semi-preparative enantioseparations were performed by a HPLC system equipped with a PerkinElmer (Norwalk, CT, USA) 200 LC pump, a Rheodyne (Cotati, CA, USA) injector, a 5 mL sample loop, a PerkinElmer LC 101 oven and Waters (Waters Corporation, Milford, USA) 484 detector. The signal was acquired and processed by the Clarity software (DataApex, Prague, the Czech Republic). Elutions were performed at 15 °C with a Chiralpak IB (250 mm x 4.6 mm, 5 mm) column, using *n*-hexane–acetone–isopropanol 100:5:1 (v/v/v); flow rate, 1 mL min^{-1} as mobile phase (Figure S14). Detection was obtained by circular dichroism (CD) at 380 nm.

Electrodeposited inherently chiral electroactive films for enantiodiscrimination tests: The conducting oligomer films were electrodeposited from the corresponding enantiopure **2** (*EN1*) or (*EN2*) monomer solutions (0.75 mM), in dichloromethane (CH_2Cl_2, Aldrich, HPLC grade) with 0.1 M Bu_4NPF_6 (Fluka, electrochemical grade) as supporting electrolyte. Electrodepositions were performed by repeated potential cycling (20 CV cycles, at 0.2 V s^{-1} scan rate on the GC disk electrode).

CV and Differential Pulse Voltammetry (DPV) experiments were performed using an Autolab PGSTAT potentiostat (Eco-Chemie, Utrecht, The Netherlands), controlled by a PC with the GPES software provided by the same manufacturer. The three-electrode V-shaped minicell (with 3 cm^3 of substrate solution) was equipped with a glassy carbon disk embedded in glass (GC, Metrohm, S = 0.031 cm^2) as working electrode, a Pt disk as counter electrode, and an aqueous saturated calomel (SCE) as reference electrode, inserted in a compartment filled with the working medium and ending with a porous frit, to avoid water and KCl leakage into the working solution. The optimized preliminary polishing procedure for the GC disk electrode consisted in treatment with a diamond powder of 1 μm diameter (Aldrich) on a wet DP-Nap cloth (Struers®). The potential values were referred to the $Fc^+|Fc$ redox measured in the same working conditions (+0.49 V *vs* SCE in CH_2Cl_2).

Acknowledgements

The authors thank the IQST (Integrated Quantum Science and Technology) at the University of Stuttgart through funding by the Carl-Zeiss-Foundation. The MIUR (Ministero dell'Istruzione, Università e Ricerca) is gratefully acknowledged for financial support. Beatrice Omiecienski is acknowledged for her help with the SEM experiments and Patrizia Mussini for scientific discussions. Vincenzo Brancaccio is acknowledged for his help in Cover Page picture design. Open access funding enabled and organized by Projekt DEAL.

Conflict of Interest

The authors declare no conflict of interest.

Keywords: 2 · 2′-biindoles · π spacer · electroactive films · oligothiophenes · mixed valence conductivity

[1] H. Shirakawa, E. J. Louis, A. G. MacDiarmid, C. K. Chiang, A. J. Heeger, *J. Chem. Soc. Chem. Commun.* **1977**, 578–580.
[2] A. J. Heeger, *Chem. Soc. Rev.* **2010**, *39*, 2354–2371.
[3] X. Sun, Y. Liu, S. Chen, W. Qiu, G. Yu, Y. Ma, T. Qi, H. Zhang, X. Xu, D. Zhu, *Adv. Funct. Mater.* **2006**, *16*, 917–925.
[4] C. Q. Ma, E. Mena-Osteritz, T. Debaerdemaeker, M. M. Wienk, R. A. J. Janssen, P. Bäuerle, *Angew. Chem. Int. Ed.* **2007**, *46*, 1679–1683; *Angew. Chem.* **2007**, *119*, 1709–1713.
[5] A. R. Murphy, J. M. J. Fréchet, *Chem. Rev.* **2007**, *107*, 1066–1096.
[6] U. Mehmood, A. Al-Ahmed, I. A. Hussein, *Renewable Sustainable Energy Rev.* **2016**, *57*, 550–561.
[7] K. Sun, S. Zhang, P. Li, Y. Xia, X. Zhang, D. Du, F. H. Isikgor, J. Ouyang, *J. Mater. Sci. Mater. Electron.* **2015**, *26*, 4438–4462.
[8] X. Fan, W. Nie, H. Tsai, N. Wang, H. Huang, Y. Cheng, R. Wen, L. Ma, F. Yan, Y. Xia, *Adv. Sci.* **2019**, *6*, 1900813.
[9] M. Wieland, C. Malacrida, Q. Yu, C. Schlewitz, L. Scapinello, A. Penoni, S. Ludwigs, *Flex. Print. Electron.* **2020**, *5*, 1–12.
[10] S. Ludwigs, Ed., *P3HT Revisited – from Molecular Scale to Solar Cell Devices*, Springer, Heidelberg, **2014**.
[11] X. Guo, A. Facchetti, *Nat. Mater.* **2020**, *19*, 922–928.
[12] J. G. Ibanez, M. E. Rincón, S. Gutierrez-Granados, M. Chahma, O. A. Jaramillo-Quintero, B. A. Frontana-Uribe, *Chem. Rev.* **2018**, *118*, 4731–4816.
[13] S. Arnaboldi, S. Grecchi, M. Magni, P. Mussini, *Curr. Opin. Electrochem.* **2018**, *7*, 188–199.
[14] F. Sannicolò, S. Rizzo, T. Benincori, W. Kutner, K. Noworyta, J. W. Sobczak, V. Bonometti, L. Falciola, P. R. Mussini, M. Pierini, *Electrochim. Acta* **2010**, *55*, 8352–8364.
[15] T. Benincori, S. Gámez-Valenzuela, M. Goll, K. Bruchlos, C. Malacrida, S. Arnaboldi, P. R. Mussini, M. Panigati, J. T. López Navarrete, M. C. Ruiz Delgado, et al., *Electrochim. Acta* **2018**, *284*, 513–525.
[16] T. Benincori, G. Appoloni, P. R. Mussini, S. Arnaboldi, R. Cirilli, E. Quartapelle Procopio, M. Panigati, S. Abbate, G. Mazzeo, G. Longhi, *Chem. A Eur. J.* **2018**, *24*, 11082–11093.
[17] F. Sannicolò, S. Arnaboldi, T. Benincori, V. Bonometti, R. Cirilli, L. Dunsch, W. Kutner, G. Longhi, P. R. Mussini, M. Panigati, et al., *Angew. Chem. Int. Ed.* **2014**, *53*, 2623–2627; *Angew. Chem.* **2014**, *126*, 2661–2665.
[18] F. Sannicolò, P. R. Mussini, T. Benincori, R. Cirilli, S. Abbate, S. Arnaboldi, S. Casolo, E. Castiglioni, G. Longhi, R. Martinazzo, et al., *Chem. A Eur. J.* **2014**, *20*, 15298–15302.
[19] S. Arnaboldi, T. Benincori, R. Cirilli, W. Kutner, M. Magni, P. R. Mussini, K. Noworyta, F. Sannicolò, *Chem. Sci.* **2015**, *6*, 1706–1711.
[20] S. Arnaboldi, T. Benincori, R. Cirilli, S. Grecchi, L. Santagostini, F. Sannicolò, P. R. Mussini, *Anal. Bioanal. Chem.* **2016**, *408*, 7243–7254.
[21] T. Benincori, S. Arnaboldi, M. Magni, S. Grecchi, R. Cirilli, C. Fontanesi, P. R. Mussini, *Chem. Sci.* **2019**, *10*, 2750–2757.
[22] S. Arnaboldi, T. Benincori, A. Penoni, L. Vaghi, R. Cirilli, S. Abbate, G. Longhi, G. Mazzeo, S. Grecchi, M. Panigati, et al., *Chem. Sci.* **2019**, *10*, 2708–2717.
[23] E. Quartapelle Procopio, T. Benincori, G. Appoloni, P. R. Mussini, S. Arnaboldi, C. Carbonera, R. Cirilli, A. Cominetti, L. Longo, R. Martinazzo, et al., *New J. Chem.* **2017**, *41*, 10009–10019.
[24] M. Hasegawa, K. Kobayakawa, H. Matsuzawa, T. Nishinaga, T. Hirose, K. Sako, Y. Mazaki, *Chem. A Eur. J.* **2017**, *23*, 3267–3271.
[25] G. Abbiati, A. Arcadi, E. Beccalli, G. Bianchi, F. Marinelli, E. Rossi, *Tetrahedron* **2006**, *62*, 3033–3039.
[26] D. Oeter, H. J. Egelhaaf, C. Ziegler, D. Oelkrug, W. Göpel, *J. Chem. Phys.* **1994**, *101*, 6344–6352.
[27] R. S. Becker, J. De Seixas Mélo, A. L. Maçanita, F. Eliseil, *J. Phys. Chem.* **1996**, *100*, 18683–18695.
[28] M. I. Nan, E. Lakatos, G. I. Giurgi, L. Szolga, R. Po, A. Terec, S. Jungsuttiwong, I. Grosu, J. Roncali, *Dyes Pigm.* **2020**, *181*, 108527.
[29] J. Roncali, *Chem. Rev.* **1997**, *97*, 173–205.
[30] J. Heinze, B. A. Frontana-Uribe, S. Ludwigs, *Chem. Rev.* **2010**, *110*, 4724–4771.
[31] C. Malacrida, A. H. Habibi, S. Gámez-Valenzuela, I. Lenko, P. S. Marqués, A. Labrunie, J. Grolleau, J. T. López Navarrete, M. C. Ruiz Delgado, C. Cabanetos, et al., *ChemElectroChem* **2019**, *6*, 4215–4228.
[32] M. Iyoda, H. Shimizu, *Chem. Soc. Rev.* **2015**, *44*, 6411–6424.
[33] T. M. Swager, *Macromolecules* **2017**, *50*, 4867–4886.

[34] T. Amemiya, K. Hashimoto, A. Fujishima, K. Itoh, *J. Electrochem. Soc.* **1991**, *138*, 2845–2850.
[35] P. Bäuerle, *Adv. Mater.* **1992**, *4*, 102–107.
[36] L. Zhang, N. S. Colella, B. P. Cherniawski, S. C. B. Mannsfeld, A. L. Briseno, *ACS Appl. Mater. Interfaces* **2014**, *6*, 5327–5343.
[37] P. Audebert, J. M. Catel, V. Duchenet, L. Guyard, P. Hapiot, G. Le Coustumer, *Synth. Met.* **1999**, *101*, 642–645.
[38] B. B. Berkes, A. S. Bandarenka, G. Inzelt, *J. Phys. Chem. C* **2015**, *119*, 1996–2003.
[39] G. Zotti, G. Schiavon, A. Berlin, G. Pagani, *Adv. Mater.* **1993**, *5*, 551–554.
[40] G. Zotti, G. Schiavon, A. Berlin, G. Pagani, *Synth. Met.* **1993**, *61*, 81–87.
[41] C. Malacrida, Y. Lu, K. Dirnberger, S. Gámez-Valenzuela, M. C. Ruiz Delgado, S. Ludwigs, *J. Mater. Chem. C* **2020**, *8*, 15393–15405.
[42] D. Ofer, R. M. Crooks, M. S. Wrighton, *J. Am. Chem. Soc.* **1990**, *112*, 7869–7879.
[43] H. John, R. Bauer, P. Espindola, P. Sonar, J. Heinze, K. Müllen, *Angew. Chem. Int. Ed.* **2005**, *44*, 2447–2451; *Angew. Chem.* **2005**, *117*, 2501–2505.
[44] D. Lee, T. M. Swager, *Chem. Mater.* **2005**, *17*, 4622–4629.
[45] G. Salinas, B. A. Frontana-Uribe, *ChemElectroChem* **2019**, *6*, 4105–4117.
[46] J. Heinze, H. John, M. Dietrich, P. Tscuncky, *Synth. Met.* **2001**, *119*, 49–52.
[47] G. Salinas, J. A. Del-Oso, P. J. Espinoza-Montero, J. Heinze, B. A. Frontana-Uribe, *Synth. Met.* **2018**, *245*, 135–143.
[48] E. F. Dalton, N. A. Surridge, J. C. Jernigan, K. O. Wilbourn, J. S. Facci, R. W. Murray, *Chem. Phys.* **1990**, *141*, 143–157.

Manuscript received: April 15, 2021
Revised manuscript received: June 4, 2021
Accepted manuscript online: June 14, 2021